Computers and Geotechnics 183 (2025) 107173

Contents lists available at ScienceDirect

Computers and Geotechnics

journal homepage: www.elsevier.com/locate/compgeo

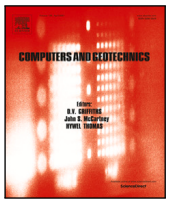

Research paper

Micropolar hypoplasticity modeling of localized deformation in mixtures of face mask chips and sand

Yu-Qi He, Zhen-Yu Yin *

Department of Civil and Environmental Engineering, The Hong Kong Polytechnic University, Kowloon, Hong Kong 999077, China
Research Centre for Nature-based Urban Infrastructure Solutions, The Hong Kong Polytechnic University, Kowloon, Hong Kong 999077, China

ARTICLE INFO

Keywords:
Soil reinforcement
Hypoplasticity
Shear band
Finite element method
Micropolar theory

ABSTRACT

This paper presents a novel micropolar-based hypoplastic model to reproduce the stress–strain relationship of face mask chips-sand mixtures (MSMs) and their localized deformation. Based on a critical state hypoplastic model, a non-polar hypoplastic model for MSMs is first developed with modifications and new features: (1) the cohesion induced by face mask chips is considered by introducing an additional stress tensor into the Cauchy stress tensor; (2) the initial stiffness variation in MSMs is described with a modified tangential modulus; and (3) the effective skeleton void ratio concept is introduced to capture the initial and critical void ratio variations in MSMs. The model is then extended to its micropolar terms by incorporating the micropolar theory, which includes an internal length parameter and a couple stress induced by particle rotation, with the advantage of overcoming the mesh dependency problem in the conventional finite element method (FEM) based simulations. Moreover, the new micropolar hypoplastic formulations are implemented into a FEM code. The onset and evolution of shear bands in MSMs are investigated by simulating a series of biaxial tests on both pure sand and MSMs. Numerical results are also compared to experimental observations, demonstrating that the developed micropolar hypoplastic model can adeptly capture the shear band propagation in MSMs and their mechanical responses.

1. Introduction

Soil reinforcement with flexible fibers is widely used in civil engineering to enhance the overall mechanical behavior of soils. Generally, those fiber-based materials include polypropylene, polyester, carbon fibers, glass fibers, biodegradable fibers, and others (Cui et al., 2018; Correia et al., 2021; Jain et al., 2023). Previous studies have shown that these fibers can significantly increase the shear strength and ductility of soils, resulting in improved resistance against failure and crack propagation (Diambra et al., 2010; Gao and Zhao, 2013; Gao et al., 2020; Ekinci et al., 2022). In recent years, due to the outbreak of the coronavirus pandemic, a considerable quantity of fiber-based disposable face masks have been stocked and caused significant environmental challenges (Zhang et al., 2022). To conserve resources and properly dispose of these face masks, few attempts have been made to add face masks into soils to improve their engineering properties. The results demonstrate that this technique can greatly improve the shear strength of soils with an optimal face mask content and a proper mask length (Xu et al., 2022; Zhang et al., 2022), which exhibits significant potential in engineering construction and disaster prevention.

Current studies mainly focus on the strength characteristics of disposable face mask chips-sand mixtures (MSMs). However, their strain localization behaviors, which play an essential role during deformations, need in-depth experimental and numerical investigations. Remarkable achievements have been made in the numerical modeling of strain localization within the framework of conventional continuum mechanics (Borja et al., 2000; Liao et al., 2021). Nevertheless, some difficulties are still involved, such as the well-known mesh dependency problem, which severely affects the thickness of shear bands in numerical simulations (Mánica et al., 2018; Li et al., 2020). Previous studies have revealed that the thickness of shear bands is closely related to the particle size (Roscoe, 1970; Scarpelli and Wood, 1982; Mühlhaus and Vardoulakis, 1987; Tatsuoka et al., 1990; Amirrahmat et al., 2019; Rattez et al., 2022), indicating that the particle size can be considered as an internal length scale of granular materials. However, such internal length is not considered in the conventional rate-independent continuum. To overcome this deficiency, extended continuum theories have been developed by introducing an internal scale parameter, e.g., micropolar theory (Tejchman, 1994), nonlocal theory (Mánica et al., 2018), and gradient theory (Triantafyllidis and Aifantis, 1986). Other attempts, for instance, the viscoplasticity concept (Loret and Prevost, 1990), have also been adopted to address the limitation.

* Corresponding author.
E-mail address: zhenyu.yin@polyu.edu.hk (Z.-Y. Yin).

https://doi.org/10.1016/j.compgeo.2025.107173
Received 15 November 2024; Received in revised form 9 January 2025; Accepted 24 February 2025
Available online 7 March 2025

These methods can be categorized as regularization techniques, and they share a common feature of controlling the thickness of shear bands through the internal length instead of the mesh size. Micropolar theory, also known as Cosserat theory (Cosserat and Cosserat, 1909), is particularly well-suited for describing granular materials, such as sand, where particle rotations play a substantial role upon loading (Wu et al., 2022). Unlike the classical continuum theory that only considers translational degrees of freedom, the micropolar theory incorporates the rotation of a material as an additional variable to describe the localized deformation (Lin, 2013). This rotation generally induces a couple stress, which represents the angular momentum and leads to a non-symmetric stress tensor (Zhu et al., 2021).

Over the past thirty years, the micropolar theory has been employed to address various boundary problems involving localized deformation within the frameworks of elastoplasticity (Tang et al., 2020) and hypoplasticity (Tejchman and Bauer, 1996). Elastoplastic constitutive models provide a comprehensive theoretical framework and a clear physical interpretation of model parameters. However, their model equations are often complex and pose challenges when applied in engineering practices and numerical implementations. The hypoplastic constitutive model offers an alternative approach to describe soil behaviors. It is developed without recourse to some concepts in elastoplasticity, such as plastic potential, yield surface, and decomposition of stains into elastic and plastic parts (Wang et al., 2018, 2020; He et al., 2023). The hypoplastic model considering the critical state proposed by Wu et al. (2017) requires only five parameters; nevertheless, it can well capture the dilatation and failure of sand with different initial densities. However, this five-parameter hypoplastic model employs a Drucker–Prager type of failure surface, resulting in consistent strength predictions under both triaxial compression and extension conditions. Von Wolffersdorff (1996) introduced the Matsuoka-Nakai failure surface into the hypolplasticity and proposed an eight-parameter hypoplastic model, providing a more robust theoretical framework of hypoplasticity for subsequent developments. Based on the basic hypoplastic frameworks by Wu et al. (2017) and Von Wolffersdorff (1996), many updated versions have been developed (Duque et al., 2020; Liao and Yang, 2021; Wang and Wu, 2021; He et al., 2022, 2023). Tejchman (1994) first introduced the micropolar theory into the hypoplastic framework to simulate shear band formation in the sand during biaxial tests. Following his pioneer work, Huang and Bauer (2003) incorporated the critical state theory into the micropolar hypoplastic model to investigate the influence of initial density on shear band thickness. In addition, the micropolar-based hypoplastic model has been further extended to study the effects of transverse anisotropy (Tejchman and Niemunis, 2006) and grain fragmentation (Bauer et al., 2019) on the evolution of shear bands in granular materials. These hypoplastic models exhibit similar micropolar terms, as the rate of the couple stress tensor is assumed to be determined by the rate of the stress tensor. An alternative way of incorporating the micropolar theory into a hypoplastic model is using complex tensor formulations. Based on this approach, Lin et al. (2015) investigated the propagation of the persistent shear band in heterogeneous granular materials.

The present work aims to develop a constitutive model of MSMs and further investigate the strain localization process in MSMs within the framework of micropolar hypoplasticity. First, a new hypoplastic model is developed to describe the mechanical behavior of MSMs. After validation, the micropolar theory is incorporated into the model with an internal length that controls the thickness of the shear band. The magnitude of this length parameter can be linked to the mean grain size of sand. We finally implement the developed micropolar hypoplastic formulations into a finite element code and simulate a series of biaxial tests on both pure sand and MSMs to investigate the shear band propagation under various loading conditions.

Notation and conventions: In this paper, second-order tensors are denoted with bold letters (e.g., **T**, **D**). The tensor multiplication rules are: $\mathbf{A}\cdot\mathbf{B} = A_{ik}B_{kj}$ and $\mathbf{A}:\mathbf{B} = A_{ij}B_{ij}$. The quantity $\|\mathbf{A}\| = \sqrt{\mathbf{A}:\mathbf{A}}$ denotes the Euclidean norm of **A**. $\mathrm{tr}\mathbf{A} = \mathbf{A}_{ii}$ refers to the trace of **A**, and $\mathbf{A}^* = \mathbf{A}\text{-}\mathbf{I}(\mathrm{tr}\mathbf{A})/3$ signifies the deviatoric part of **A**, where **I** is a second-order unity tensor.

Table 1
Physical parameters for pure sand and MSM samples.

Materials	d_{50}/mm	e_{max}	e_{min}	C_u	C_c	Face mask size/mm
Pure sand	0.78	0.81	0.56	1.28	0.84	–
MSM-I	0.78	–	–	1.28	0.84	10 × 10
MSM-II	0.78	–	–	1.28	0.84	12 × 3
MSM-III	0.78	–	–	1.28	0.84	20 × 5

2. Mechanical behaviors of MSMs

First, a series of consolidation-drained triaxial tests on MSMs under different confining pressures (p_c = 50, 100, and 200 kPa) and initial densities (D_r = 90% and 60%) were conducted to investigate the mechanical behavior of MSMs. The tested sand is Fujian standard sand with a mean grain size of d_{50} = 0.78 mm. The face mask used is a polypropylene-based material with low density. Detailed properties regarding the tested sand and face mask chips can be found in our previous experimental work (Xu et al., 2024).

During the tests, the face mask chips were uniformly mixed with sand to create MSM samples, which have a cylindrical shape with a height of 200 mm and a diameter of 100 mm. The MSM samples included three mask chip dimensions: 10 mm × 10 mm (labeled as MSM-I), 12 mm × 3 mm (labeled as MSM-II), and 20 mm × 5 mm (labeled as MSM-III). The mass ratio of face mask chips to the pure sand is 0.5% in each sample. The specific gravities of pure sand and the face mask chip are 2.65 and 1.0, respectively. Other physical parameters are summarized in Table 1, where e_{max} and e_{min} represent the maximum and minimum void ratios of the pure sand, while C_u and C_c denote the uniformity coefficient and coefficient of curvature of the pure sand, respectively.

Fig. 1 shows the measured stress–strain and volumetric strain relationships for pure sand and MSMs. Note that due to the space constraints, only the test result with D_r = 90% at a confining pressure of 100 kPa is given in this section. The result indicates that: (1) Both pure sand and MSMs exhibit strain softening at the same confining pressure with an identical initial density of D_r = 90%. However, MSMs present a higher peak strength compared to pure sand, and the increase in strength at an axial strain of 20% is smaller than that at the peak state, indicating that mask chips will experience a certain degree of damage as loading progresses. Moreover, it can be observed that MSM-III exhibits the highest strength, followed by MSM-I and MSM-II. Compared to MSM-I and MSM-III, the mask chip in MSM-II is the smallest in size but the largest in number, causing the formation of fiber-weakening surface that limits the enhancement of strength, i.e., an excess of fibers in the sand will increase the void ratio at the interface between fibers and sand, thereby reducing the density of the sand and subsequently weakening its strength. Additionally, strip mask chips (MSM-III) induce higher strength compared to a square one (MSM-I). (2) Compared to pure sand, MSMs present smaller initial stiffness, and the axial strain corresponding to the peak state of MSMs is also greater than that of pure sand. This observation is consistent with the findings of Manohar and Anbazhagan (2021), where rubber-like materials can enhance the strength of soil at a larger axial strain. (3) MSMs exhibit smaller volumetric strains compared to pure sand. This is because the internal structure of the sand skeleton is altered by the face mask chips, as a result, the void ratio is changed. These observations reveal the primary mechanical behaviors of MSMs, which will contribute to the development of constitutive models for MSMs.

In order to further reveal the reinforcement mechanism of MSMs from the perspective of strength parameters, Mohr circles of pure sand and MSMs under various confining pressures at peak states were plotted in Fig. 2. In which ϕ_p refers to the internal friction angle at the peak state and c_0 is the initial cohesion. The results demonstrate that upon incorporating mask chips into the sand, there is only little change in the internal friction angle of the sand, while the cohesion experiences

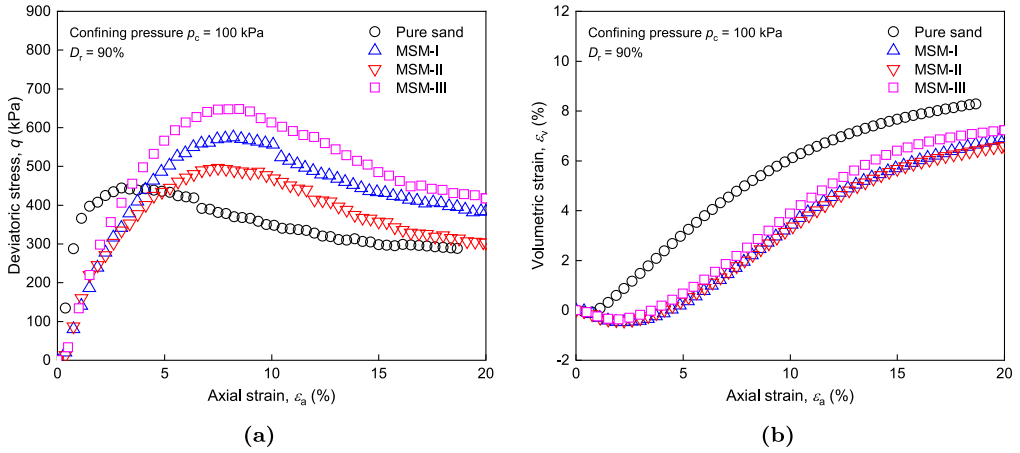

Fig. 1. The mechanical behaviors of pure sand and MSMs: (a) stress–strain curves; and (b) volumetric strain curves.

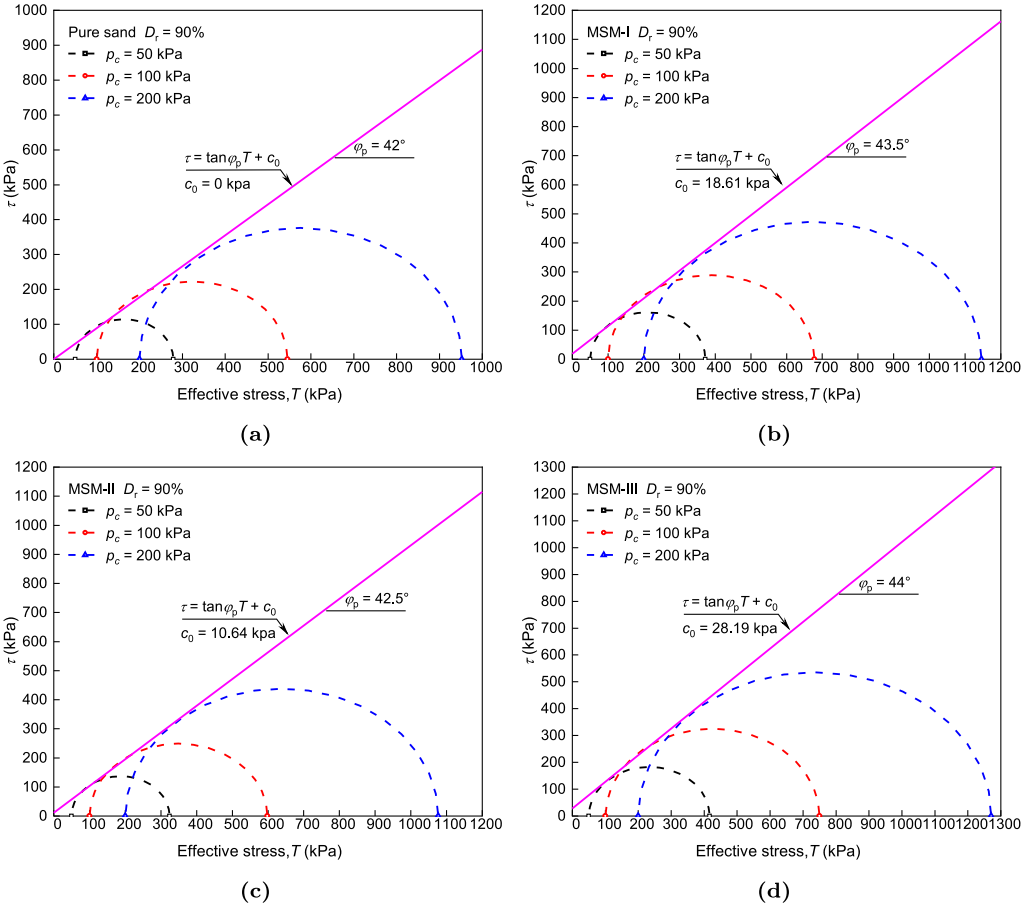

Fig. 2. Shear strength envelopes of pure sand and MSMs at peak state: (a) Pure sand; (b) MSM-I; (c) MSM-II; and (d) MSM-III.

a significant increase. This indicates that mask chips primarily enhance the soil strength by boosting its cohesion (Xu et al., 2022). Moreover, experimental observations have shown that the face mask chip in the sand undergoes specific damage during loading, which implies that the cohesion caused by the face mask chip will gradually diminish as the loading progresses.

3. Hypoplastic model for MSMs

3.1. A basic hypoplastic model for sand

To develop a hypoplastic model for MSMs, let us consider the following simple hypoplastic constitutive equation proposed by Wu et al. (2017):

$$\mathring{\mathbf{T}} = C_1(\mathrm{tr}\mathbf{T})\mathbf{D} + C_2(\mathrm{tr}\mathbf{D})\mathbf{T} + C_3\frac{\mathrm{tr}(\mathbf{TD})}{\mathrm{tr}\mathbf{T}}\mathbf{T} + f_e C_4(\mathbf{T}+\mathbf{T}^*)\|\mathbf{D}\| \tag{1}$$

where $\mathring{\mathbf{T}}$ is the Jaumann stress rate, $\mathbf{T}$ is the Cauchy stress tensor, and $\mathbf{D}$ is the strain rate tensor. C_i $(i = 1, 2, 3, 4)$ are four material constants that can be determined by the initial tangential modulus E_i, the Poisson's ratio ν_i, and the critical friction angle φ (Wu and Bauer, 1994). The density function f_e accounts for stress history through

$$f_e = \left(\frac{e}{e_{crt}}\right)^{\alpha} \tag{2}$$

in which e and e_{crt} are the current void ratio and critical void ratio, respectively, and α is a model parameter that controls the degree of strain softening. By incorporating the density function f_e, both dense and loose sands can be modeled with one set of model parameters.

3.2. A new hypoplastic model for MSMs

The aforementioned investigations have shown that the face mask chip primarily enhances soil strength by increasing its cohesion, with only a little change observed in the friction angle. In the hypoplastic framework, this cohesion can be introduced into the Cauchy stress tensor as follows

$$\mathring{\mathbf{T}} = C_1(\mathrm{tr}\check{\mathbf{T}})\mathbf{D} + C_2(\mathrm{tr}\mathbf{D})\check{\mathbf{T}} + C_3\frac{\mathrm{tr}(\check{\mathbf{T}}\mathbf{D})}{\mathrm{tr}\check{\mathbf{T}}}\check{\mathbf{T}} + f_e C_4(\check{\mathbf{T}}+\check{\mathbf{T}}^*)\|\mathbf{D}\| \tag{3}$$

where $\check{\mathbf{T}} = \mathbf{T} + \mathbf{C}$ with $\mathbf{C}$ refers to the cohesion tensor induced by face mask chips, which can be expressed as

$$\mathbf{C} = c_0\mathbf{I} \tag{4}$$

where c_0 means the initial cohesion induced by the face mask chip, it can be measured through triaxial compression tests. Upon loading, we assume that the cohesion completely vanishes when the deformation is sufficiently large and propose the following evolution law:

$$\dot{c}_0 = -d_t\|\mathbf{D}\|c_0 \tag{5}$$

where d_t controls the damage rate.

Moreover, the inclusion of face mask chips in sand can influence the internal structure of the sand skeleton. As a result, the effective void ratio of sand may be different from the global void ratio. This difference can be described by the concept of effective skeleton void ratio (Diambra et al., 2013; Gao et al., 2020). Based on this concept, the relationship between the global void ratio e and the effective void ratio e^s of sand can be assumed as

$$e^s = (1 + \chi c_f)e \tag{6}$$

where $c_f = v_f/v_s$ denotes the volume content ratio with v_f and v_s being the volume contents of the face mask chip and pure sand, respectively. χ is a model parameter that can be either positive or negative. $\chi > 0$ indicates an increased void ratio, resulting in a looser sand sample. While $\chi < 0$ means a decreased effective void ratio, leading to a denser sand sample. Whether $\chi > 0$ or $\chi < 0$ depends on the sample preparation methods. In addition, c_f can be expressed in terms of the weight content ratio w_f through

$$c_f = \frac{v_f}{v_s} = \frac{w_f G_s v_s/G_f}{v_s} = \frac{w_f G_s}{G_f} \tag{7}$$

in which G_s and G_f represent the specific gravities of pure sand and the face mask chip, respectively. The Eq. (6) can be rewritten as

$$e^s = (1 + \chi w_f G_r)e \tag{8}$$

with $G_r = G_s/G_f$ denoting the ratio of the specific gravity of sand to face mask chips.

The critical state line is modified as

$$e^s_{crt} = e_\Gamma \exp\left[-\lambda\left(\frac{p^s}{p_a}\right)^{\zeta}\right] \tag{9}$$

where $p^s = p + c_0$ with $p = -\mathrm{tr}\mathbf{T}/3$ refers to the modified mean stress composed of the host sand and face mask parts. e_Γ, λ, and ζ are model parameters and p_a stands for the atmospheric pressure (p_a = 101 kPa). Therefore, the density function f_e can be updated as

$$f^s_e = \left(\frac{e^s}{e^s_{crt}}\right)^{\alpha} \tag{10}$$

Previous studies have shown that MSMs generally exhibit lower initial stiffness compared to a pure sand sample. To describe this stiffness reduction, the tangential modulus E_i is modified as follows

$$\bar{E}^m_i = \bar{E}_i \exp\left(r_s\sqrt{\frac{c_0}{p_a}}\right)^{-1} \tag{11}$$

where $\bar{E}_i = E_i/T_c$ refers to the normalized tangential modulus, with E_i and T_c denote the initial tangential modulus and the consolidation pressure, respectively. r_s is a model parameter that controls the stiffness reduction magnitude. As a result, a new hypoplastic model for MSMs can be written as

$$\mathring{\mathbf{T}} = C_1(\mathrm{tr}\check{\mathbf{T}})\mathbf{D} + C_2(\mathrm{tr}\mathbf{D})\check{\mathbf{T}} + C_3\frac{\mathrm{tr}(\check{\mathbf{T}}\mathbf{D})}{\mathrm{tr}\check{\mathbf{T}}}\check{\mathbf{T}} + f^s_e C_4(\check{\mathbf{T}}+\check{\mathbf{T}}^*)\|\mathbf{D}\| \tag{12}$$

Furthermore, according to Liu et al. (2021), the hypoplastic model developed from the framework in Eq. (1) generally underestimates soil dilatation. To remedy this, the new model in Eq. (12) is updated as

$$\mathring{\mathbf{T}} = C_1(\mathrm{tr}\check{\mathbf{T}})\mathbf{D} + (1 - f^s_e)C_2(\mathrm{tr}\mathbf{D})\check{\mathbf{T}} + C_3\frac{\mathrm{tr}(\check{\mathbf{T}}\mathbf{D})}{\mathrm{tr}\check{\mathbf{T}}}\check{\mathbf{T}} + f^s_e C_4(\check{\mathbf{T}}+\check{\mathbf{T}}^*)\|\mathbf{D}\| \tag{13}$$

As mentioned above, the material constants C_i $(i = 1, 2, 3, 4)$ can be calibrated with the initial tangential modulus E_i, the Poisson's ratio ν_i, and the critical friction angle φ (Zhu et al., 2024). In the present work, the initial tangential modulus E_i is modified to reproduce the stiffness variation of MSMs (see Eq. (11)). As a result, the material constants C_i now can be determined by $\bar{E}_i$, ν_i, φ, r_s, and c_0. The relationship between these two sets of parameters is analytically derived from a triaxial compression test as follows:

$$C_1 = -\frac{b\bar{E}_i}{3(1+\nu_i)} \tag{14a}$$

$$C_2 = C_1\left(\frac{3\nu_i + a\sqrt{1+2\nu_i^2}}{1-2\nu_i} - \frac{a^2}{3}\right) \tag{14b}$$

$$C_3 = a^2 C_1 \tag{14c}$$

$$C_4 = aC_1 \tag{14d}$$

where $a = [\sqrt{3}(3 - \sin\varphi)]/[2\sqrt{2}\sin\varphi]$ and $b = \exp(r_s\sqrt{c_0/p_a})^{-1}$. In the following, the parameters $\bar{E}_i$, ν_i, and φ will be used for simplicity.

3.3. Model parameters

The developed hypoplastic model for MSMs requires 12 parameters that can be classified into 3 groups:

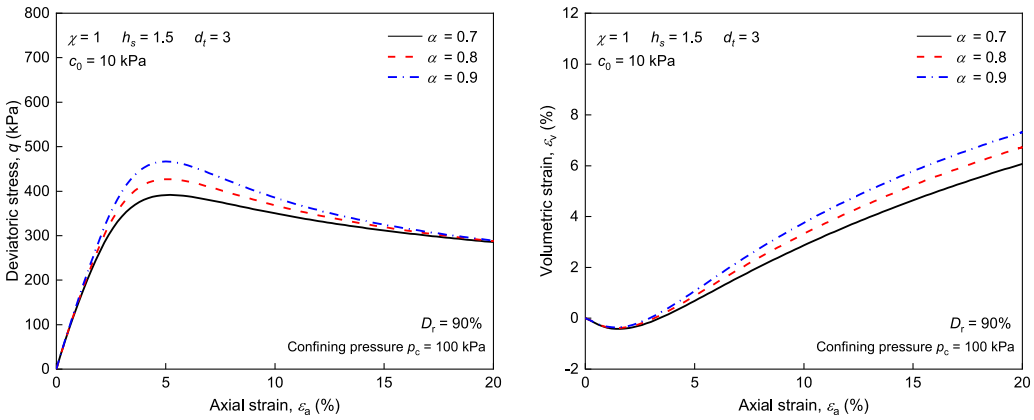

Fig. 3. The effect of parameter α on the model responses: (a) stress–strain curves; and (b) volumetric strain curves.

Table 2
Material parameters for model calibration.

Parameters	$\bar{E}_i$	ν_i	φ (°)	e_Γ	λ	ζ	w_f
Values	230	0.25	30	0.84	0.026	0.8	0.005

(1) Three basic parameters: $\bar{E}_i$, ν_i, and φ;

(2) Four critical state parameters: e_Γ, λ, ζ, and α;

(3) Five additional parameters related to the face mask chips: c_0, χ, w_f, r_s, and d_t.

The three basic parameters $\bar{E}_i$, ν_i, and φ can be determined through a triaxial compression test. The critical parameters e_Γ, λ and ζ can be obtained through the critical state line of the sand. α controls the softening rate and can be identified by trial and error. The additional parameter c_0 refers to the cohesion induced by the face mask chip, which can be determined through Mohr circles of MSMs under different effective confining pressures. w_f is the weight content ratio of the face mask chip. The remaining parameters χ, r_s, and d_t require curve fitting.

The effect of four basic parameters and the critical parameters e_Γ, λ, and ζ on the model is the same as those in the model proposed by Wu et al. (2017). In the following, therefore, we will discuss the effect of the parameters α, c_0, χ, r_s, and d_t on the model responses through a series of drained triaxial compression simulations. In simulations, trial values of these parameters will be used and other parameters are listed in Table 2. The initial void ratio is adopted as $e = 0.585$. The specific gravities G_s and G_f are 2.65 and 1.0, respectively.

Fig. 3 demonstrates that α mainly controls the peak strength and softening rate of the model but does not affect the critical strength. A larger α will lead to a higher peak strength and a faster softening rate. Generally, the value of α falls between 0.5 and 1.

Fig. 4 shows the effects of newly added parameters c_0, χ, r_s, and d_t on the model responses. It can be observed that an increase in c_0 will give rise to an increase in the overall strength of the model, while the initial stiffness and the volumetric deformation are decreased. The parameters χ and r_s control the peak strength and initial stiffness of the model, respectively. The parameter d_t controls the strength degradation rate of the model.

3.4. Model validation

In this section, we will validate our model by comparing model predictions to experimental data on the pure sand and MSMs. The physical parameters of the pure sand and MSMs are summarized in Table 1. Table 3 provides the material parameters for model simulations. Note that the determination of the parameters c_0 can be found in Section 2.

Figs. 5 and 6 present a comparison between experimental and numerical drained triaxial tests on pure sand and MSMs under different confining pressures (p_c = 50, 100, and 200 kPa) and initial densities (D_r = 90% and 60%). Compared to pure sand, MSMs show a slight decrease in volumetric strains, along with higher shear strength and lower initial stiffness. These behaviors can be accurately predicted by the developed model. Furthermore, the predicted results agree well with the experimental data at lower stress levels but slightly underestimate the residual stress at a confining pressure of 200 kPa, especially in the case of D_r = 60%. Overall, the developed hypoplastic model can effectively capture the strength and deformation characteristics of pure sand and MSMs with various initial densities under different stress levels.

4. Development of micropolar hypoplastic model

4.1. Micropolar hypoplastic formulations

Unlike the conventional continuum, a material point in the micropolar continuum has both translational and rotational degrees of freedom. Fig. 7 shows these degrees of freedom in 2-D problems.

The presence of rotational degrees of freedom gives rise to a non-symmetric strain rate tensor, which can be mathematically represented as

$$\mathbf{D}^m = \mathbf{D} + \mathbf{W} - \delta\boldsymbol{\omega} \tag{15}$$

where $\mathbf{D}^m$ is the non-symmetric strain rate tensor and $\boldsymbol{\omega}$ refers to the micro-rotation tensor. δ is a permutation operator. The symmetric strain rate tensor $\mathbf{D}$ and spin tensor $\mathbf{W}$ are related to the velocity gradient as follows:

$$\mathbf{D} = [\nabla\mathbf{v} + (\nabla\mathbf{v})^{\mathrm{T}}]/2, \qquad \mathbf{W} = [\nabla\mathbf{v} - (\nabla\mathbf{v})^{\mathrm{T}}]/2 \tag{16}$$

where $\mathbf{v}$ is the velocity vector with ∇ denoting the gradient operator. The superscript T is a transposition operator.

In addition, the curvature rate tensor that describes the spatial derivation of the micro-rotation can be written as

$$\mathbf{K} = \nabla\boldsymbol{\omega} \tag{17}$$

Generally, there are two approaches to incorporating the micropolar theory into the hypoplastic framework. The first approach involves obtaining the couple stress rate through a simple analogy with the stress rate in the non-polar hypoplastic model (Tejchman and Bauer, 1996). The second one is using complex tensor formulations to derive the Jaumann stress rate and couple stress rate (Lin, 2013). In the present work, we will adopt complex tensor formulations to derive the micropolor terms of the developed model for MSMs.

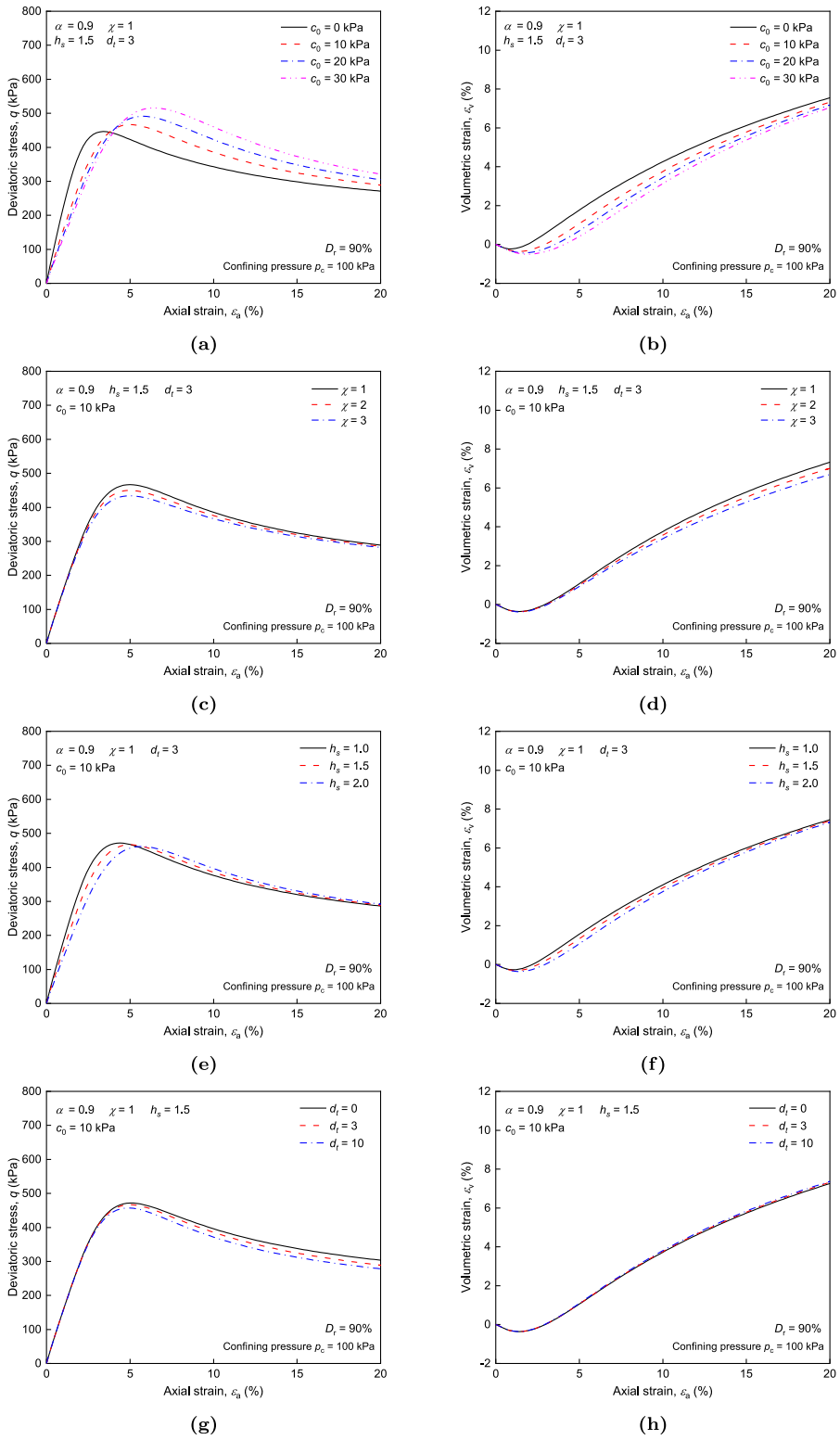

Fig. 4. The effect of parameters c_0, χ, r_s, and d_t on the model responses: (a), (b) c_0; (c), (d) χ; (e), (f) r_s; and (g), (h) d_t.

Table 3
Model parameters for numerical simulations.

Materials	$\bar{E}_i$	ν_i	φ/°	e_Γ	e	λ	ζ	α	c	χ	r_s	d_t
Pure sand	230	0.25	32	0.84	0.585/0.66	0.026	0.8	0.9	0	0	0	0
MSM-I	–	0.25	32	0.84	–	0.026	0.8	0.9	18.61	0.5	2	3
MSM-II	–	0.25	32	0.84	–	0.026	0.8	0.9	10.64	3	2	3
MSM-III	–	0.25	32	0.84	–	0.026	0.8	0.9	28.19	0.1	1.4	3

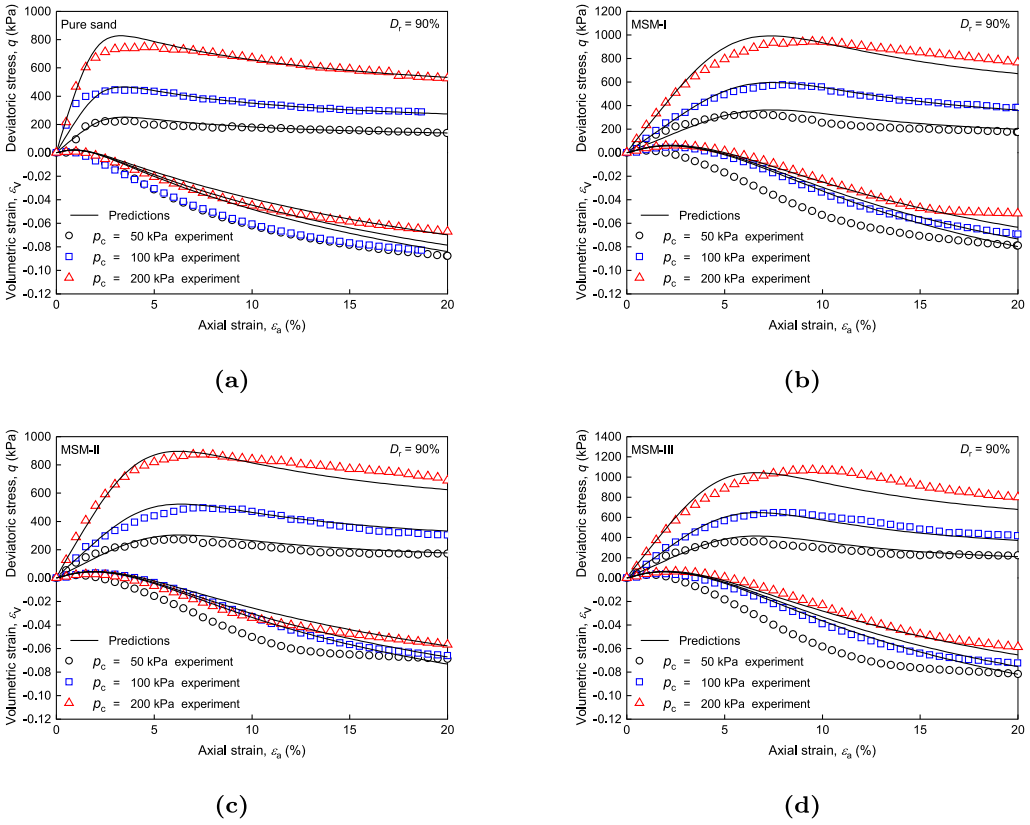

Fig. 5. Comparison between experimental and numerical drained triaxial tests on face mask chips reinforced Fujian sand with D_r = 90%: (a) Pure sand; (b) MSM-I; (c) MSM-II; and (d) MSM-III.

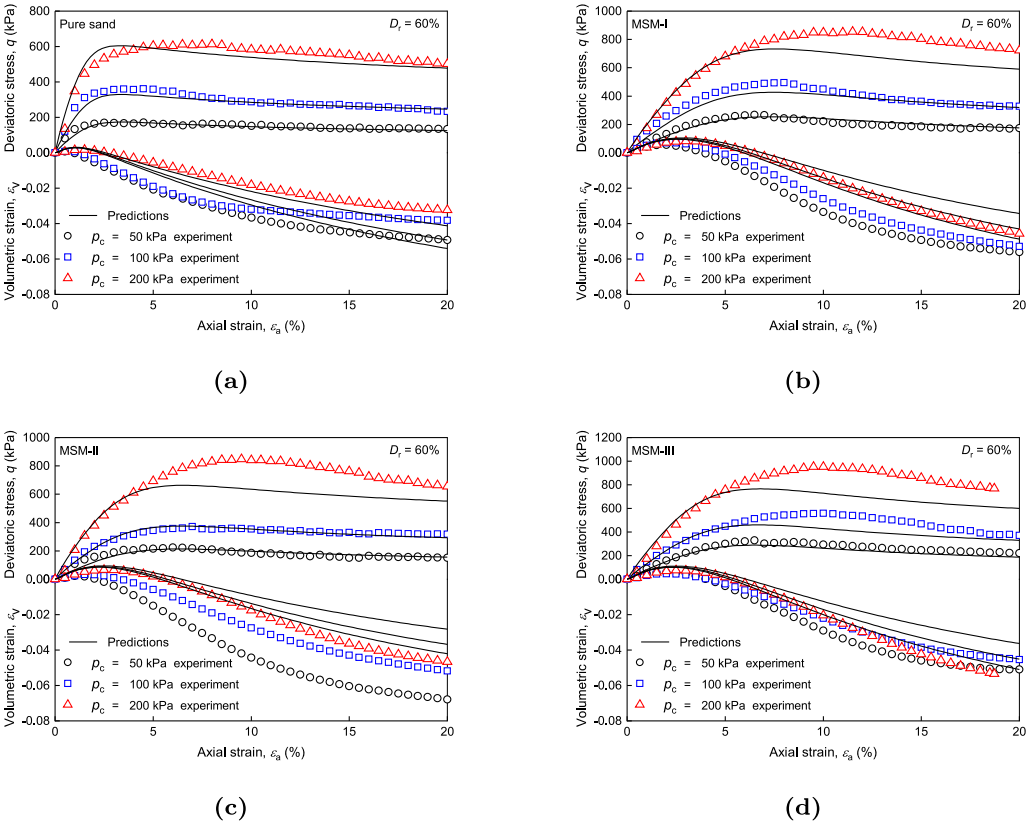

Fig. 6. Comparison between experimental and numerical drained triaxial tests on face mask chips reinforced Fujian sand with D_r = 60%: (a) Pure sand; (b) MSM-I; (c) MSM-II; and (d) MSM-III.

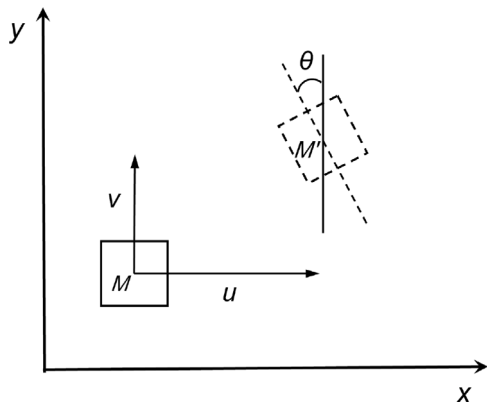

Fig. 7. Degrees of freedom in a 2-D micropolar continuum.

Mathematical derivation based on the developed model (13) yields the following micropolar hypoplastic constitutive relations:

$$\mathring{\check{\mathbf{T}}} = C_1 \mathrm{tr}(\check{\mathbf{T}})\mathbf{D}^m + f_d C_2 \mathrm{tr}(\mathbf{D}^m)\check{\mathbf{T}} + C_3 F \check{\mathbf{T}} + f_e^s C_4 \sqrt{(\|\mathbf{D}^m\|^2 + l^2\|\mathbf{K}\|)^2} \times (\check{\mathbf{T}} + \check{\mathbf{T}}^*) \tag{18}$$

and

$$\mathring{\mathbf{M}} = C_1 l^2 \mathrm{tr}(\check{\mathbf{T}})\mathbf{K} + f_d C_2 \mathrm{tr}(\mathbf{D}^m)\mathbf{M} + C_3 F \mathbf{M} + 2 f_e^s C_4 \sqrt{(\|\mathbf{D}^m\|^2 + l^2\|\mathbf{K}\|)^2}\mathbf{M} \tag{19}$$

where $\mathring{\check{\mathbf{T}}}$ is the new stress rate and $\mathring{\mathbf{M}}$ is the couple stress rate with

$$F = \frac{\mathrm{tr}\check{\mathbf{T}}\mathbf{D}^m - \mathrm{tr}\mathbf{M}\mathbf{K}}{\mathrm{tr}\check{\mathbf{T}}} \quad \textit{and} \quad f_d = 1 - f_e^s \tag{20}$$

In the above micropolar hypoplastic constitutive equations, the stress tensor $\check{\mathbf{T}}$ and material constants C_i, as well as the evolution of the void ratio e, remain unchanged from the hypoplastic model Eq. (13). Only one additional parameter l, known as internal length, is introduced to account for the thickness of the shear band. Generally, the value of l depends on the mean grain size of the sand particle. The newly formulated $\mathbf{K}$, $\mathbf{M}$, and $\mathring{\mathbf{M}}$ are skew-symmetric tensors. Detailed mathematical derivation process can be found in the literature (Lin, 2013).

4.2. Finite element implementation

We proceed to implement the developed model and the micropolar element into the finite element code ABAQUS for further investigations. In finite element analysis, it is common to convert the strong form of a partial differential equation (governing equation) into its weak form. The weak form is then discretized, resulting in a problem of solving a group of linear equations.

For a micropolar body $\mathscr{B}$ with a boundary surface $\partial\mathscr{B}$ and an outward unit normal vector $\mathbf{n}$, we assume that the body $\mathscr{B}$ has Dirichlet and Neumann boundaries denoted as $\partial\mathscr{B}_g$ and $\partial\mathscr{B}_h$, respectively. Within the body $\mathscr{B}$, there exists the stress $\check{\mathbf{T}}$, the couple stress $\mathbf{M}$, the body force $\mathbf{b}$, and the body couple force $\mathbf{c}$. On the boundary $\partial\mathscr{B}_h$, there exists the force traction vector $\check{\mathbf{T}}_h$ and the couple traction vector $\mathbf{M}_h$. The governing equations include

$$\rho\frac{D\mathbf{v}}{Dt} - \nabla\cdot\check{\mathbf{T}} - \rho\mathbf{b} = \mathbf{0} \tag{21}$$

for balance of linear momentum, and

$$\rho\frac{D(\mathbf{J}\cdot\boldsymbol{\omega})}{Dt} - \nabla\cdot\mathbf{M} - \rho\mathbf{J}\cdot\mathbf{c} - \delta(\check{\mathbf{T}}) = \mathbf{0} \tag{22}$$

for balance of angular momentum, where ρ denotes the mass density, D/D_t is the material time derivative, and $\mathbf{J}$ is the moment of inerita tensor. δ is a permutation operator which leads to

$$\delta(\check{\mathbf{T}}) = [\check{T}_{32} - \check{T}_{32}, \check{T}_{13} - \check{T}_{31}, \check{T}_{21} - \check{T}_{12}]^\mathsf{T} \tag{23}$$

To obtain the weak form of the governing equations, we first multiply Eqs. (21) and (22) by an arbitrary weighting function

$$\mathscr{W} = \{\boldsymbol{\eta}, \boldsymbol{\vartheta} \mid \eta_i, \vartheta_i \in H\} \tag{24}$$

which results in

$$\int_{\mathscr{B}} \boldsymbol{\eta}\cdot\left(\rho\frac{D\mathbf{v}}{Dt} - \nabla\cdot\check{\mathbf{T}} - \rho\mathbf{g}\right)\mathrm{d}V = 0 \tag{25}$$

and

$$\int_{\mathscr{B}} \boldsymbol{\vartheta}\cdot\left[\rho\frac{D(\mathbf{J}\cdot\boldsymbol{\omega})}{Dt} - \nabla\cdot\mathbf{M} - \rho\mathbf{J}\cdot\mathbf{c} - \delta(\check{\mathbf{T}})\right]\mathrm{d}V = 0 \tag{26}$$

Then, integrating by parts and using the divergence theorem, the weak form can be obtained as

$$\int_{\mathscr{B}} \boldsymbol{\eta}\cdot\rho\frac{D\mathbf{v}}{Dt}\mathrm{d}V + \int_{\mathscr{B}} (\nabla\boldsymbol{\eta})^\mathsf{T} : \check{\mathbf{T}}\mathrm{d}V = \int_{\mathscr{B}} \boldsymbol{\eta}\cdot\rho\mathbf{g}\mathrm{d}V + \int_{\partial\mathscr{B}_h} \boldsymbol{\eta}\cdot\check{\mathbf{T}}_h\mathrm{d}A \tag{27}$$

for linear momentum, and

$$\int_{\mathscr{B}} \boldsymbol{\vartheta}\cdot\rho\frac{D(\mathbf{J}\cdot\boldsymbol{\omega})}{Dt}\mathrm{d}V + \int_{\mathscr{B}} (\nabla\boldsymbol{\vartheta})^\mathsf{T} : \mathbf{M}\mathrm{d}V - \int_{\mathscr{B}} \boldsymbol{\vartheta}\cdot\delta(\check{\mathbf{T}})\mathrm{d}V = \int_{\mathscr{B}} \boldsymbol{\vartheta}\cdot\rho\mathbf{J}\cdot\mathbf{c}\mathrm{d}V + \int_{\partial\mathscr{B}_h} \boldsymbol{\vartheta}\cdot\mathbf{M}_h\mathrm{d}A \tag{28}$$

for angular momentum.

To obtain the element stiffness matrix, we need to determine the partial derivatives of Eqs. (18) and (19):

$$\frac{\partial\mathring{\check{T}}_{ij}}{\partial D^m_{kl}} = C_1\Phi I_{ijkl} + C_2\check{T}_{ij}\delta_{kl} + C_3\check{T}_{ij}\check{T}_{kl}\Phi^{-1} + C_4(\check{T}_{ij} + \check{T}^*_{ij})\mathscr{D}_{kl} \tag{29a}$$

$$\frac{\partial\mathring{M}_{ij}}{\partial D^m_{kl}} = C_2\check{T}_{ij}\delta_{kl} + C_3 M_{ij}\check{T}_{kl}\Phi^{-1} + 2C_4 M_{ij}\mathscr{D}_{kl} \tag{29b}$$

$$\frac{\partial\mathring{\check{T}}_{ij}}{\partial K_{kl}} = -C_3\check{T}_{ij}M_{kl}\Phi^{-1} + C_4(\check{T}_{ij} + \check{T}^*_{ij})\mathscr{K}_{kl} \tag{29c}$$

$$\frac{\partial\mathring{M}_{ij}}{\partial K_{kl}} = C_1 l^2\Phi I_{ijkl} - C_3 M_{ij}M_{kl}\Phi^{-1} + 2C_4 M_{ij}\mathscr{K}_{kl} \tag{29d}$$

in which $\Phi = \mathrm{tr}\check{\mathbf{T}}$. $\mathscr{D}_{kl}$ and $\mathscr{K}_{kl}$ can be expressed as

$$\mathscr{D}_{kl} = \frac{D^m_{kl}}{\sqrt{\|\mathbf{D}^m\|^2 + l^2\|\mathbf{K}\|^2}} \quad \textit{and} \quad \mathscr{K}_{kl} = \frac{l^2 K_{kl}}{\sqrt{\|\mathbf{D}^m\|^2 + l^2\|\mathbf{K}\|^2}} \tag{30}$$

and I_{ijkl} is a fourth-order identity tensor with

$$I_{ijkl} = \frac{1}{2}(\delta_{ik}\delta_{jl} + \delta_{jk}\delta_{il}) \tag{31}$$

For a plane strain problem, Eqs. (29a), (29b), (29c), and (29d) are (5×5), (5×2), (2×5), and (2×2) matrices, respectively. As a result, the stiffness matrix of the developed micropolar hypoplastic model for MSMs can be written as

$$\boldsymbol{\mathcal{M}} = \begin{bmatrix} \frac{\partial\mathring{\check{T}}_{ij}}{\partial D^m_{kl}} & \frac{\partial\mathring{M}_{ij}}{\partial D^m_{kl}} \\ \frac{\partial\mathring{\check{T}}_{ij}}{\partial K_{kl}} & \frac{\partial\mathring{M}_{ij}}{\partial K_{kl}} \end{bmatrix} \tag{32}$$

The developed micropolar hypoplastic model is further integrated by giving a time step $\triangle t$:

$$\check{\mathbf{T}}_{n+1} = \check{\mathbf{T}}_n + \boldsymbol{\mathcal{M}}\mathbf{D}\triangle t \tag{33}$$

4.3. Mesh independency

As previously mentioned, the classical finite element analysis suffers from pathological mesh dependency in strain localization problems (Mánica et al., 2018). The micropolar theory presents a distinct advantage over classical continuum theory by adeptly capturing shear bands through particle rotations rather than translations. The magnitude of the rotation is determined solely by a predefined internal length parameter. As a result, the micropolar theory exhibits a solution

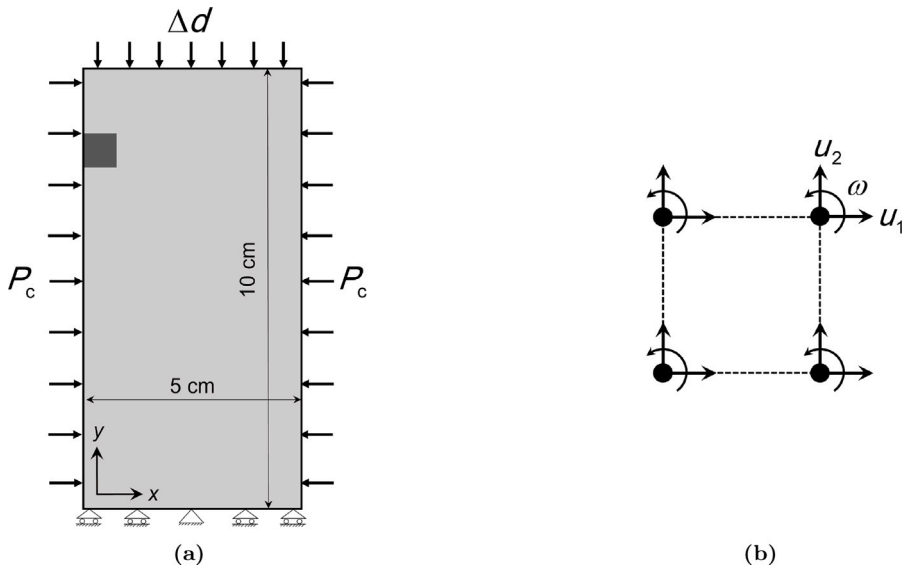

Fig. 8. A 2-D plane strain numerical model: (a) boundary conditions; and (b) a four-node element.

independent of the mesh size, providing a substantial advantage in accurately describing the formation and evolution of shear bands. In what follows, we proceed to establish a 2-D plane strain numerical model with five finite element meshes to validate the developed micropolar hypoplastic model.

As illustrated in Fig. 8, the plane strain model has dimensions of 50 mm in width and 100 mm in height. The model is discretized using five different mesh sizes: 2.9 mm (with a total of 561 elements), 2.2 mm (with a total of 1035 elements), 1.5 mm (with a total of 2211 elements), 1.2 mm (with a total of 3486 elements), and 1.0 mm (with a total of 5000 elements). Each element consists of four nodes, and each node has two translational degrees of freedom and one rotational degree of freedom. To simulate the formation of shear bands, a weak element with a higher void ratio of $e = 0.7$ is introduced, as represented by the dashed area in Fig. 8(a). The internal length parameter is set to $l = 0.2$ mm. The loading process consists of two steps, i.e., consolidation and axial compression. During the first step, a uniform pressure of 100 kPa is applied to the top boundary and two lateral boundaries to simulate an isotropic consolidation configuration. For the axial compression step, a downward displacement is applied to the top boundary while the horizontal displacement and rotation remain free. The two lateral boundaries are all free to displace and rotate. Additionally, in both steps, the bottom nodes are constrained in vertical displacements and rotations, while the center node of the bottom boundary is pinned to model a fully symmetric loading condition. The model parameters for pure sand in Table 3 are used for this set of simulations. Note that the effect of the face mask chip is not considered in this case since our primary purpose is to verify the mesh independency of the developed model.

Since the micropolar element (user-defined element) is considered in ABAQUS, a post-processing technique is necessary to improve the numerical visualization. In this work, the MATLAB code was chosen for processing the numerical result due to its simplicity. Fig. 9 shows the post-processed contour plot of the rotation magnitude obtained from the above numerical simulations. The result reveals that the shear band predicted by the micropolar theory is not totally independent of the mesh size. For instance, the shear band cannot be adequately captured in the case of 561 elements, suggesting that the mesh is too coarse to obtain an appropriate solution. However, as the number of elements increases, the mesh independency becomes more evident. It can be observed that the width and angle of the shear bands under different mesh sizes exhibit a high degree of consistency when the element count exceeds 2211. The only difference is that the rotation magnitude increases with increasing the element numbers. Furthermore, the width of the shear band is approximately 2.8 mm, which aligns with the research findings of Lin (2013), suggesting that the width of the shear band is around 10~15 times the internal length. Some discerning readers may notice that the black mesh in Fig. 9 does not fully align with the colored geometry. This misalignment arises due to the contour plot was generated by overlaying the black mesh and the colored geometry, in which the black mesh was portrayed based on the horizontal and vertical displacements of nodes. However, the colored geometry was depicted according to the rotational magnitude of nodes in addition to their horizontal and vertical displacements. As a result, a small section of the colored geometry may not align precisely with the black mesh. Despite this discrepancy, it is deemed acceptable as we mainly focus on investigating the mesh independency of the micropolar approach.

Fig. 10 presents the stress–strain curves in numerical simulations with different mesh sizes. The result demonstrates that with 561 elements, the predicted stress–strain curve may exhibit slight differences compared to the results obtained with the other four cases, and the strength of the sample decreases slightly as the mesh size decreases. However, these stress–strain curves exhibit high consistency when the number of elements exceeds a certain threshold (2211 in this case).

5. Analysis of strain localization in MSMs

In this section, we will investigate the shear band formation and evolution in MSMs under a plain strain condition based on the developed micropolar hypoplastic model. The numerical results will be compared to experimental data for further validation.

5.1. Numerical biaxial models

In the experimental test, the MSM sample was prepared in a rectangular shape measuring 70 mm × 70 mm × 160 mm and subjected to loading at confining pressures of 50 and 100 kPa. The physical properties of the tested sand and face mask chips remain consistent with those described in Section 2. The corresponding finite element (FE) model has a 2-D shape with dimensions of 70 mm in width and 160 mm in height, consisting of 2800 elements generated with a mesh size of 2 mm. The internal length that governs the width of the shear band is set to $l = 0.78$ mm, the same as the mean grain size of the tested sand. The initial void ratio is set to $e = 0.585$, resulting in a relative

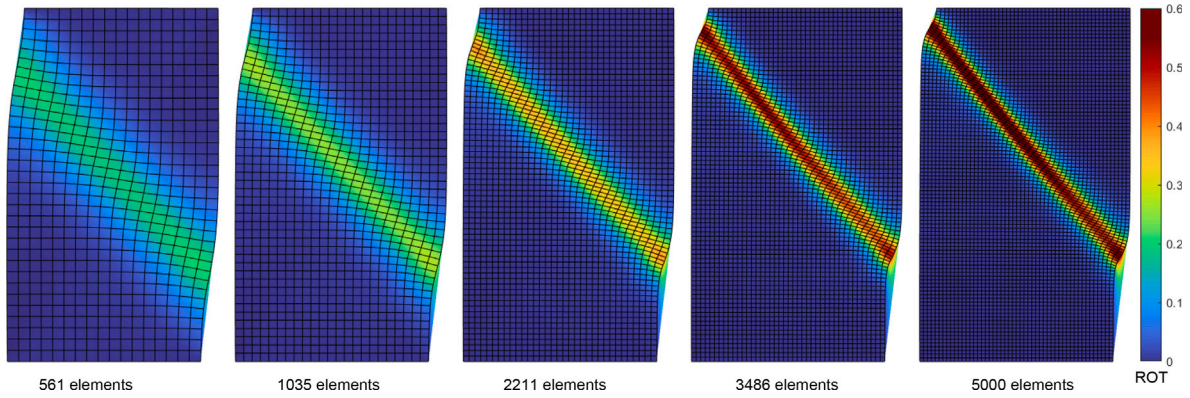

Fig. 9. Contour of the rotation magnitude at an axial strain of ε_a = 7% in plane strain tests with different mesh sizes (color bar in radians).

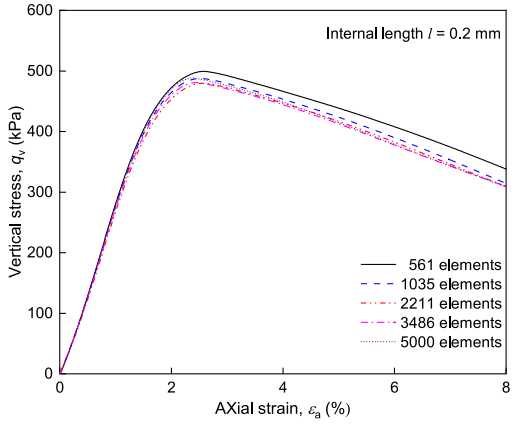

Fig. 10. Stress–strain curves in numerical plane strain test simulations.

density of D_r = 90%. The remaining model parameters are consistent with Table 3.

It is well known that the onset of the shear band is influenced by weak elements. To accurately simulate the shear band patterns observed in experimental tests, the numerical FE model will consider three different locations for weak elements, as depicted in Fig. 11. Note that cases 1 and 2 are employed to simulate a single type of shear band, while case 3 induces an X-shaped shear band. In case 3, the weak element is located at the central axis of the sample, which enforces a fully symmetric loading configuration. In all cases, the void ratio of the weak element is defined as $e = 0.7$.

5.2. Shear band evolution in MSMs

Fig. 12 provides the experimental and numerical stress–strain curves for MSM-II at a confining pressure of 50 kPa. To further reveal the dynamic evolution of shear bands in MSMs, three different stress states during the loading process, i.e., hardening, peak, and stable, are selected for detailed analyses. These selected states are marked as A, B, and C in experimental results, and a superscript "$*$" is used to represent the corresponding numerical results. Herein, the stable state means the shear band pattern remains unchanged rather than indicating a static stress state.

It can be seen that both experimental and numerical deviatoric stresses demonstrate a gradual softening trend after reaching the peak stress point. The predicted hardening point A* and stable point C* closely align with the experimental results A and C, respectively. While the predicted peak stress point B* slightly surpasses the experimental counterpart, and the predicted axial strain corresponding to the peak point is also a little bit overestimated. Overall, a good agreement between numerical predictions and experimental data is observed. Next, we will compare the shear bands at these selected points in numerical simulations and experiments, focusing primarily on analyzing changes in the inclination angles and widths of the shear bands.

Fig. 13 presents the propagation of shear bands in both experimental observations and numerical simulations at a confining pressure of 50 kPa. The results reveal that during the progressive failure of MSMs, the evolution of the shear band undergoes dynamic changes, with variations in thickness and shape at different strain stages. As strain increases, the MSM sample will initially enter the hardening stage, during which the sample shows very slight deformation, and the shear band starts to form at the weak point of the sample, although it is not clearly observable. When the sample reaches its peak strength, the shear band will evolve into a distinct band-like structure within a narrow region and can be clearly observed, as shown in Fig. 13 at axial strains of 6.3% and 3.8%. After the peak stress point, the MSM sample enters the softening stage, where the internal structure of the sample undergoes dramatic rearrangement, and its deformation becomes increasingly concentrated within the shear band; consequently, the thickness of the shear band gradually decreases. Once reaching the stable state, the shear band exhibits a preferred orientation and maintains a constant width, as shown in Fig. 13 at axial strains of 11.4% and 10.8%.

In addition, we can observe that the onset of the shear band is significantly delayed in the MSM compared to the pure sand sample. For example, in the pure sand, the axial strain at which the shear band can be clearly observed is 2.9%, while it is 5.8% in the MSM sample (in experiments). The result demonstrates that face mask chips can prevent the development of localized deformation in sand. Moreover, in experiments, the inclination angles of the shear band for pure sand and MSM-II are 55° and 52°, respectively. This suggests that face mask chips may slightly reduce the inclination angle of the shear band in the sand; however, this phenomenon is not able to be replicated in our numerical simulations, where the inclination angles of the shear band for pure sand and MSM-II are 49° and 48°, respectively. The predicted shear band width is around 14 mm in both pure sand and MSM samples, consistent with experimental observations, suggesting that face mask chips do not alter the width of the shear band in the sand.

Fig. 14 presents the numerical and experimental deviatoric stress–strain curves for pure sand and MSMs at a confining pressure of 100 kPa. The results demonstrate that the developed model reasonably captures the initial stiffness, peak stress, and post-peak behavior of MSMs. In experiments, the stress–strain curve of the pure sand approaches the critical state with a rapid softening rate at an axial strain of 12%. However, in numerical simulations, the stress–strain curve does not reach a complete critical state. This is due to the fact that in finite element simulations, a larger deformation (12% in this case) can lead

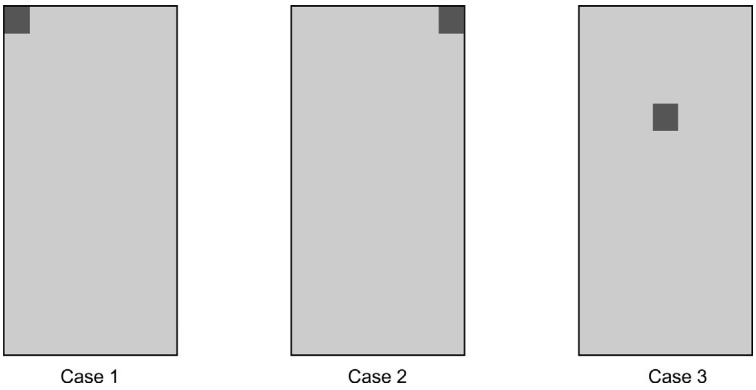

Fig. 11. Different weak element locations.

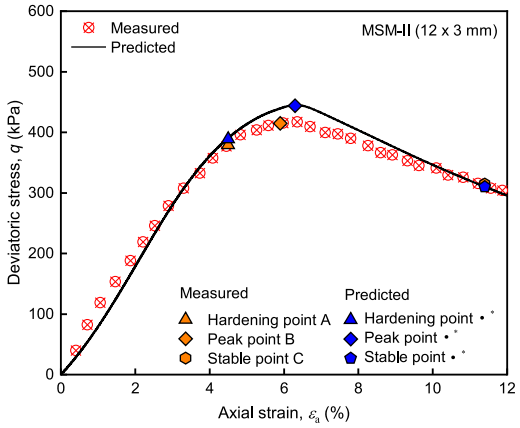

Fig. 12. Stress–strain curves for pure sand and MSM-II at a confining pressure of 50 kPa.

to mesh distortion or overlapping, leading to the termination of calculations. Nonetheless, such discrepancies are acceptable, as the shear band has fully formed within the 12% axial strain range. Furthermore, we can observe that after adding mask chips to the pure sand, the peak stress is significantly increased, and a larger axial strain is required to reach the peak stress. This indicates that the addition of mask chips to the sand can slow down the occurrence of strain localization, as the shear band becomes prominent at the peak state according to the previous discussion.

Fig. 15(a) provides the shear band at the stable state measured in experiments for pure sand and MSMs at a confining pressure of 100 kPa. It can be seen that all samples exhibit distinct shear bands with various patterns after loading. Notably, an X-shaped shear band is observed in the case of MSM-II, where the weak point is located at the center of the sample. Fig. 15(b) depicts the contour plot of rotation magnitude calculated from numerical simulations. Obviously, we can conclude that the rotation of sand particles also concentrates within the shear band during loading. The corresponding displacement magnitude ($U = \sqrt{u^2 + v^2}$) in numerical simulations is portrayed in Fig. 15(c). The result shows that the predicted displacement is almost the same as that measured in experimental tests. Furthermore, comparing Figs. 15(b) and (c), it is observed that the shear band represented by particle rotation is more visually apparent than those represented by displacement variables, which demonstrates the advantage of the micropolar theory in the quantitative description of shear band thickness.

In Fig. 15, both experimental and numerical results show that pure sand exhibits a single type of shear band. However, in the case of MSMs, either a single shear band or an X-shaped one can be observed. From a sample preparation perspective, the initial boundary condition of pure sand is non-symmetric since the weak point is not located at the center of the sample. This non-symmetric weak point will cause the upper boundary to translate during the loading process. As a result, a persistent single shear band is formed, with its initiation point determined by the location of the weak element. In the case of MSMs, the internal structure of the host sand is altered due to the incorporation of face mask chips, which may randomly change the location of the weak point. Therefore, both a single shear band with varying initiation points and an X-shaped shear band can be observed in MSMs. Some discerning readers may notice that although the predicted shear bands have nearly identical widths and inclinations (around 12 mm and 49°), the colors of the shear bands, representing the rotation magnitude, vary. This is because incorporating face mask chips into the sand enhances the soil's resistance to deformation, indicating that the interaction between mask chips and sand particles can effectively limit the development of strain localization. Moreover, the rotation magnitude of particles within the X-shaped shear band is minimal due to the opposing rotation directions of particles in two crossed bands, thereby constraining the particle rotation during loading.

5.3. Rotation magnitude in shear band

Fig. 16 shows the rotation magnitude within the shear band at confining pressures of 50 kPa and 100 kpa. The results illustrate a significant decrease in the rotation magnitude of sand particles when reinforced with face mask chips, indicating that face mask chips can effectively prevent the progression of strain localization in sand. There are two reasons contributing to this observation: (1) The rough or textured surfaces of face mask chips may create additional resistance to particle rotations. (2) The presence of face mask chips can alter the interactions between sand particles, thereby affecting their movements.

Moreover, according to the stress–strain curves presented in Fig. 14, we can conclude that the rotational velocity of sand particles is almost zero before reaching the peak stress. However, once the sand enters the softening stage, the rotation of sand particles rapidly increases. Such observation reveals that in the micropolar approach the rotation only occurs when the stress or strain field becomes non-uniform. This differs from the discrete element method, where particle rotation can be observed from the onset of loading. Additionally, there is a nearly linear relationship between the magnitude of particle rotation and axial displacement after the peak stress state. This relationship can be observed in Fig. 16(b), where positive values indicate clockwise rotations and negative values represent counterclockwise rotations. Note that an X-shaped shear band is formed in the MSM-I sample. In this case, the rotational displacement of sand particles within the two crossed shear bands has the same magnitude but in opposite directions. As a result, the shear band is not observed at the intersection point of the two crossed shear bands, where the rotational displacement equals zero.

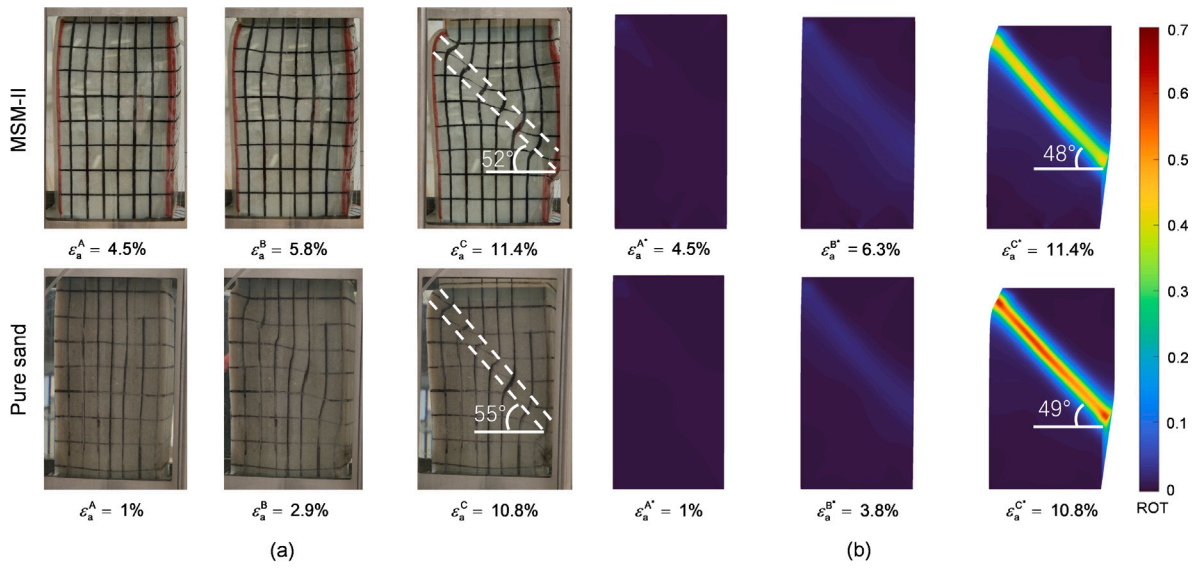

Fig. 13. Experimental and numerical shear bands for pure sand and MSM-II at a confining pressure of 50 kPa: (a) experimental observations; and (b) contour of the rotation magnitude (color bar in radians).

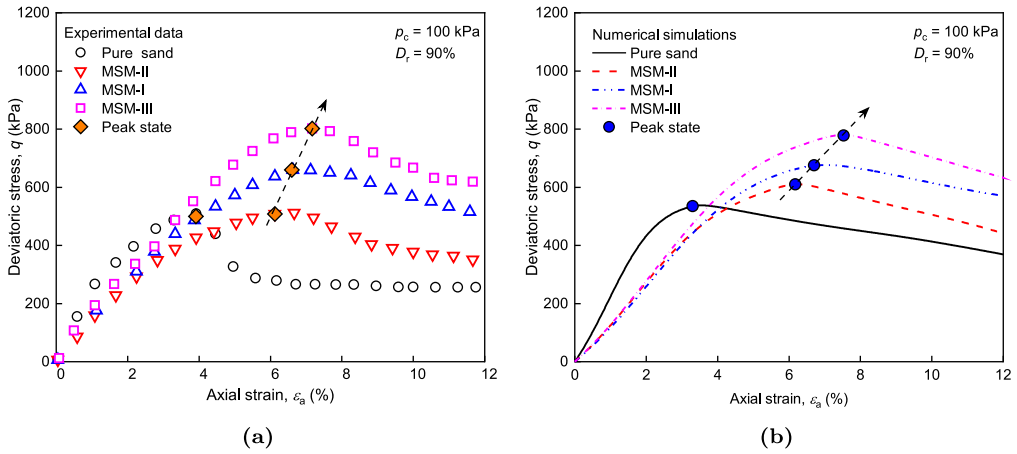

Fig. 14. Experimental and numerical stress–strain curves for pure sand and MSMs at a confining pressure of 100 kPa: (a) experimental data; and (b) numerical predictions.

5.4. Shear band orientation and thickness

The orientation and thickness are two crucial variables when describing shear bands in granular materials. Typically, the orientation of shear bands can be categorized into two limiting values. The upper limit is determined by Coulomb's theory, which suggests that the orientation of the shear band coincides with the inclination of the plane where the maximum ratio of shear to normal stress is observed:

$$\theta_C = 45° + \frac{\varphi_c}{2} \tag{34}$$

where θ_C denotes Coulomb's angle and φ_c is the internal friction angle. Roscoe's criterion provides the lower limit of the shear band and can be expressed as

$$\theta_R = 45° + \frac{\psi_f}{2} \tag{35}$$

where θ_R is Roscoe's angle and ψ_f refers to the dilation angle at failure.

Previous studies have demonstrated that the accuracy of both theories depends not only on grain size but also on various factors such as boundary conditions, pressure, initial void ratio, particle shape, and others (Alshibli and Sture, 2000). To provide a more precise description of the shear band orientation, Arthur et al. (1977) proposed an intermediate relationship between Coulomb's and Roscoe's solutions:

$$\theta_A = 45° + \frac{\varphi_c + \psi_f}{4} \tag{36}$$

where θ_A is Arthur's angle.

The thickness of the shear band in granular materials is closely related to the grain size. Numerous experimental and numerical investigations have demonstrated that smaller grain sizes cause narrower shear bands, while larger grain sizes result in thicker shear bands (Sadrekarimi and Olson, 2010). Specifically, the thickness of a shear band is typically around 10~17 times the mean grain size d_{50} (Rattez et al., 2022). This relationship is generally non-unique and can be influenced by various factors, including particle shape, initial density, grain size, etc. Such behavior can be explained using the micropolar theory, which considers the rotation of particles as the driving mechanism for shear band formation. In soils with larger grain sizes, the rotation of particles leads to a significant deformation, thereby producing a thicker shear band.

The orientation and thickness of the persistent shear band measured in experimental tests are demonstrated in Fig. 15. Fig. 17 provides their comparison with theoretical solutions and numerical simulations. Overall, the results indicate that the orientation and thickness of shear bands in sand remain relatively unchanged after reinforcement with face mask

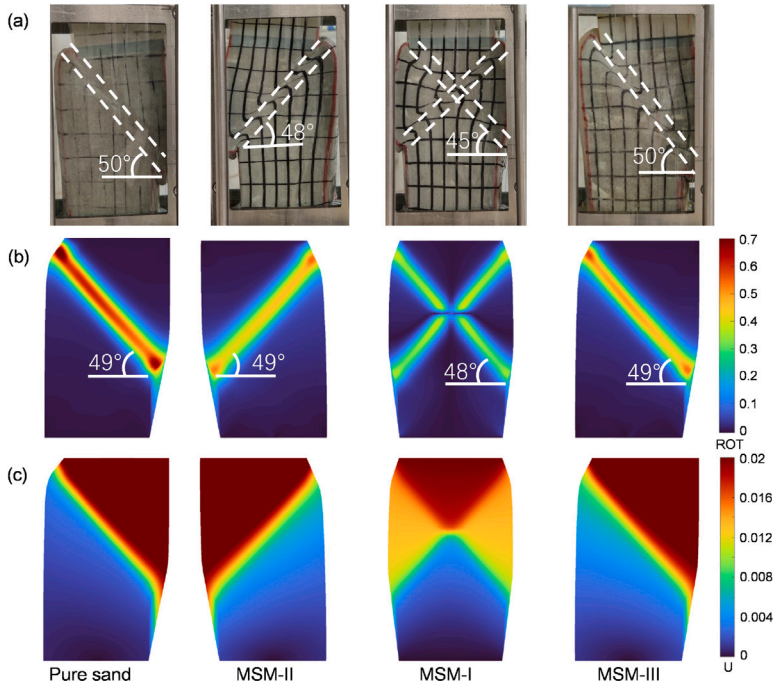

Fig. 15. Experimental and numerical shear bands for pure sand and MSMs at a confining pressure of 100 kPa: (a) experimental observations; (b) contour of the rotation magnitude (color bar in radians); and (c) contour of the displacement magnitude (color bar in mm).

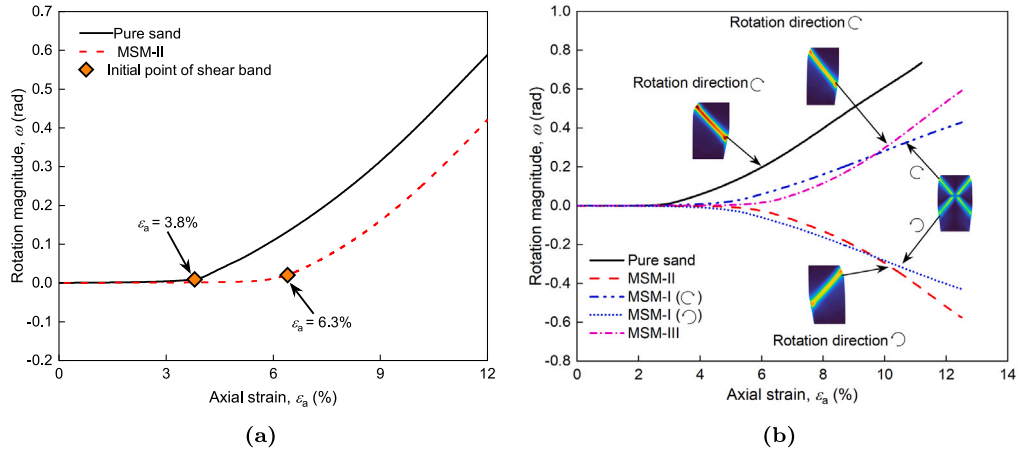

Fig. 16. Rotation magnitude within the shear band at different confining pressures: (a) 50 kPa; and (b) 100 kPa.

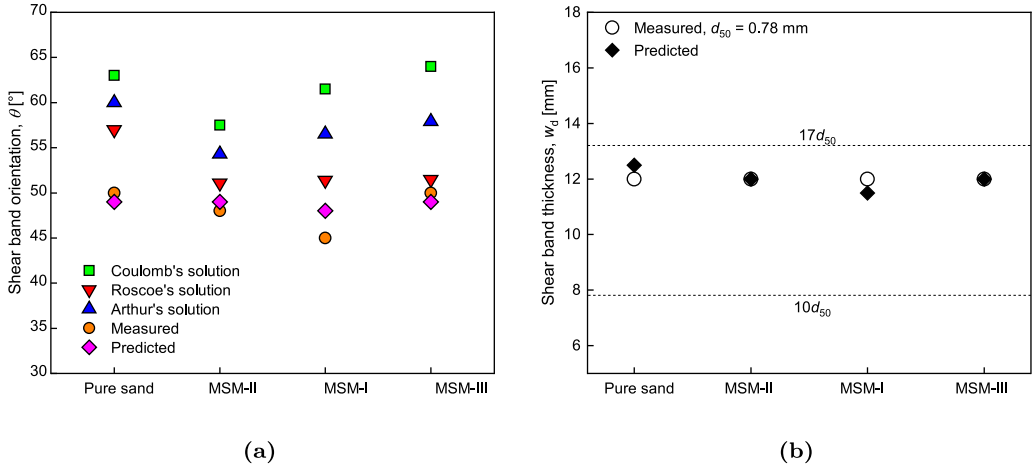

Fig. 17. Shear band orientation and thickness of pure sand and MSMs at a confining pressure of 100 kPa: (a) orientation; and (b) thickness.

chips. The experimental measurements show that the orientation of shear bands in all the samples ranges from 50~60 degrees, aligning closer with the prediction of Roscoe's theory. Among all the samples, the MSM-I sample exhibits the smallest orientation at 45 degrees. This can be attributed to the presence of the X-shaped shear band, which restricts the sliding of shear bands and results in smaller inclination angles. The numerical results predicted by the developed model are in good agreement with experimental observations, which show an orientation of approximately 49 degrees for both pure sand and MSM samples. Furthermore, the thicknesses of shear bands for pure sand and MSM samples in experimental tests are approximately 12 mm, around 15 times the mean grain size ($d_{50} = 0.78$ mm). In numerical simulations, the thicknesses of shear bands for pure sand, MSM-I, MSM-II, and MSM-III samples are approximately 12.5, 12, 11.5, and 12 mm, respectively. These values closely match the experimental results.

6. Conclusions

This paper presents a novel hypoplastic model for mask chips-sand mixtures (MSMs), which accounts for the effect of mask chips by introducing an additional stress tensor into the Cauchy stress tensor. After experimental validation, the developed model was further enriched by incorporating the micropolar theory and implemented into a finite element code to investigate the dynamic propagation of shear bands in MSMs under 2-D conditions. Numerical simulations were compared to experimental observations, demonstrating that the developed micropolar model can reasonably predict the onset and evolution of shear bands in MSMs. The main conclusions are summarized as follows:

(1) The developed hypoplastic model can effectively predict the strength and deformation characteristics of pure sand and MSMs. Compared to pure sand, MSMs exhibit higher strength and deformation resistance but lower initial stiffness. The mask chips primarily increase the strength of the sand by enhancing its cohesion, with very little changes in the internal friction angle.

(2) The micropolar theory overcomes the mesh dependency problem in the conventional finite method. However, in practical computations, a very coarse mesh size can lead to a non-unique solution. Therefore, selecting an appropriate mesh size is crucial for applying the micropolar theory in numerical simulations.

(3) In MSMs, shear bands initially form at the weak point of the sample and become distinctly observable at the peak stress state. During the strain softening phase, their thicknesses decrease continuously and concentrate within a narrow region. The shear band eventually evolves into a single or an X-shaped structure with a constant thickness and inclination, which depends on the location of the weak point in the sample.

(4) Incorporating mask chips into sand causes friction between the mask chips and sand particles, thereby preventing sand particles from rotating upon loading. This significantly enhances the deformation resistance of sand and prevents the development of strain localization under loading. Moreover, the incorporation of mask chips into sand does not alter the inclination and thickness of the shear band.

(5) The developed hypoplastic model can reasonably predict the thickness and shape of shear bands. However, there may be some discrepancies in the predicted inclination of shear bands compared to experimental results. In experiments, the inclination of shear bands shows slight variations among different samples. In numerical simulations, these inclinations remain nearly constant. This is because the developed micropolar hypoplastic model only considers the thickness of the shear band but does not account for inclination-related parameters.

CRediT authorship contribution statement

Yu-Qi He: Writing – original draft, Methodology, Formal analysis, Data curation, Conceptualization. **Zhen-Yu Yin:** Writing – review & editing, Supervision, Project administration, Methodology, Funding acquisition, Conceptualization.

Declaration of competing interest

On behalf of all authors, they declare that they have no known competing financial interests or personal relationships that could have appeared to influence the work reported in this manuscript.

Acknowledgments

This research was financially supported by the Research Grants Council (RGC) of the Hong Kong Special Administrative Region Government of China (Grant No. : 15226822), and the Research Centre for Nature-based Urban Infrastructure Solutions at The Hong Kong Polytechnic University.

Data availability

Data will be made available on request.

References

Alshibli, K.A., Sture, S., 2000. Shear band formation in plane strain experiments of sand. J. Geotech. Geoenviron. Eng. 126 (6), 495–503.
Amirrahmat, S., Druckrey, A.M., Alshibli, K.A., Al-Raoush, R.I., 2019. Micro shear bands: Precursor for strain localization in sheared granular materials. J. Geotech. Geoenviron. Eng. 145 (2), 04018104.
Arthur, J.R.F., Dunstan, T., Al-Ani, Q.A.J.L., Assadi, A., 1977. Plastic deformation and failure in granular media. Géotechnique 27 (1), 53–74.
Bauer, E., Safikhani, S., Li, L.K., 2019. Numerical simulation of the effect of grain fragmentation on the evolution of microstructure quantities. Meccanica 54, 631–642.
Borja, R.I., Regueiro, R.A., Lai, T.Y., 2000. FE modeling of strain localization in soft rock. J. Geotech. Geoenviron. Eng. 126 (4), 335–343.
Correia, N.S., Rocha, S.A., Lodi, P.C., McCartney, J.S., 2021. Shear strength behavior of clayey soil reinforced with polypropylene fibers under drained and undrained conditions. Geotext. Geomembr. 49 (5), 1419–1426.
Cosserat, E.M., Cosserat, F., 1909. Théorie des Corps Déformables. Hermann et Fils, Paris, Librairie Scientifique A.
Cui, H., Jin, Z., Bao, X., Tang, W., Dong, B., 2018. Effect of carbon fiber and nanosilica on shear properties of silty soil and the mechanisms. Constr. Build. Mater. 189, 286–295.
Diambra, A., Ibraim, E., Russell, A.R., Wood, D.M., 2013. Fibre reinforced sands: from experiments to modelling and beyond. Int. J. Numer. Anal. Methods Geomech. 37 (15), 2427–2455.
Diambra, A., Ibraim, E., Wood, D.M., Russell, A.R., 2010. Fibre reinforced sands: Experiments and modelling. Geotext. Geomembr. 28 (3), 238–250.
Duque, J., Mašín, D., Fuentes, W., 2020. Improvement to the intergranular strain model for larger numbers of repetitive cycles. Acta Geotech. 15, 3593–3604.
Ekinci, A., Ferreira, P.M.V., Rezaeian, M., 2022. The mechanical behaviour of compacted lambeth-group clays with and without fibre reinforcement. Geotext. Geomembr. 50 (1), 1–19.
Gao, Z., Lu, D., Huang, M., 2020. Effective skeleton stress and void ratio for constitutive modeling of fiber-reinforced sand. Acta Geotech. 15, 2797–2811.
Gao, Z., Zhao, J., 2013. Evaluation on failure of fiber-reinforced sand. J. Geotech. Geoenviron. Eng. 139 (1), 95–106.
He, Y.Q., Liao, H.J., Wu, W., Wang, S., 2023. Hypoplastic modeling of inherent anisotropy in normally and overconsolidated clays. Acta Geotech. 18 (12), 6315–6333.
He, Y.Q., Wang, S., Liao, H.J., Wu, W., 2022. A hypoplastic constitutive model for structured soils. Comput. Geotech. 151, 104935.
Huang, W.X., Bauer, E., 2003. Numerical investigations of shear localization in a micro-polar hypoplastic material. Int. J. Numer. Anal. Methods Geomech. 27 (4), 325–352.
Jain, A., Mittal, S., Shukla, S.K., 2023. Use of polyethylene terephthalate fibres for mitigating the liquefaction-induced failures. Geotext. Geomembr. 51 (1), 245–258.
Li, K.Q., Li, D.Q., Liu, Y., 2020. Meso-scale investigations on the effective thermal conductivity of multi-phase materials using the finite element method. Int. J. Heat Mass Transfer 151, 119383.
Liao, D., Yang, Z.Y., 2021. Hypoplastic modeling of anisotropic sand behavior accounting for fabric evolution under monotonic and cyclic loading. Acta Geotech. 16 (7), 2003–2029.
Liao, D., Yang, Z.X., Xu, T.T., 2021. J2-deformation-type soil model coupled with state-dependent dilatancy and fabric evolution: Multiaxial formulation and FEM implementation. Comput. Geotech. 129, 103674.
Lin, J., 2013. Linking DEM with Micropolar Continuum. (Ph.D. thesis). Institut für Geotechnik, Universität für Bodenkultur, Vienna, Austria.

Lin, J., Wu, W., Borja, R.I., 2015. Micropolar hypoplasticity for persistent shear band in heterogeneous granular materials. Comput. Methods Appl. Mech. Engrg. 289, 21–43.
Liu, J., Wang, S., Jiang, M.J., Wu, W., 2021. A state-dependent hypoplastic model for methane hydrate-bearing sands. Acta Geotech. 16, 77–91.
Loret, B., Prevost, J.H., 1990. Dynamic strain localization in elasto-(visco-) plastic solids, Part 1. General formulation and one-dimensional examples. Comput. Methods Appl. Mech. Engrg. 83 (3), 247–273.
Mánica, M.A., Gens, A., Vaunat, J., Ruiz, D.F., 2018. Nonlocal plasticity modelling of strain localisation in stiff clays. Comput. Geotech. 103, 138–150.
Manohar, D.R., Anbazhagan, P., 2021. Shear strength characteristics of geosynthetic reinforced rubber-sand mixtures. Geotext. Geomembr. 49 (4), 910–920.
Mühlhaus, H.B., Vardoulakis, I., 1987. The thickness of shear bands in granular materials. Géotechnique 37 (3), 271–283.
Rattez, H., Shi, Y., Sac-Morane, A., Klaeyle, T., Mielniczuk, B., Veveakis, M., 2022. Effect of grain size distribution on the shear band thickness evolution in sand. Géotechnique 72 (4), 350–363.
Roscoe, K.H., 1970. The influence of strains in soil mechanics. Géotechnique 20 (2), 129–170.
Sadrekarimi, A., Olson, S.M., 2010. Shear band formation observed in ring shear tests on sandy soils. J. Geotech. Geoenviron. Eng. 136 (2), 366–375.
Scarpelli, G., Wood, D.M., 1982. Experimental observations of shear patterns in direct shear tests. In: Proceedings of the IUTAM Conference on Deformation and Failure of Granular Materials. Delft, pp. 472–484.
Tang, H., Wei, W., Liu, F., Chen, G., 2020. Elastoplastic Cosserat continuum model considering strength anisotropy and its application to the analysis of slope stability. Comput. Geotech. 117, 103–235.
Tatsuoka, F., Nakamura, S., Huang, C., Tani, K., 1990. Strength anisotropy and shear band direction in plane strain tests of sand. Soils Found. 30 (1), 35–54.
Tejchman, J., 1994. Numerical study on localized deformation in a Cosserat continuum. In: Proceedings of 8th International Conference on Computer Methods and Advances in Geomechanics. Balkema, Rotterdam.
Tejchman, J., Bauer, E., 1996. Numerical simulation of shear band formation with a polar hypoplastic constitutive model. Comput. Geotech. 19 (3), 221–244.
Tejchman, J., Niemunis, A., 2006. FE-studies on shear localization in an anistropic micro-polar hypoplastic granular material. Granul. Matter 8, 205–220.
Triantafyllidis, N., Aifantis, E.C., 1986. A gradient approach to localization of deformation, I. Hyperelastic materials. J. Elasticity 16 (3), 225–237.
Von Wolffersdorff, P.A., 1996. A hypoplastic relation for granular materials with a predefined limit state surface. Mech. Cohesive- Frict. Mater. 1 (3), 251–271.
Wang, S., Wu, W., 2021. A simple hypoplastic model for overconsolidated clays. Acta Geotech. 16 (1), 21–29.
Wang, S., Wu, W., He, X.Z., Cui, D.S., 2018. Numerical integration and fe implementation of a hypoplastic constitutive model. Acta Geotech. 13 (6), 1265–1281.
Wang, S., Wu, W., Zhang, D.C., Kim, J.R., 2020. Extension of a basic hypoplastic model for overconsolidated clays. Comput. Geotech. Comput. Geotech. 123, 103486.
Wu, W., Bauer, E., 1994. A simple hypoplastic constitutive model for sand. Int. J. Numer. Anal. Methods Geomech. 18 (12), 833–862.
Wu, W., Lin, J., Wang, X.T., 2017. A basic hypoplastic constitutive model for sand. Acta Geotech. 12 (6), 1373–1382.
Wu, M., Wu, F., Wang, J., 2022. Particle shape effect on the shear banding in DEM-simulated sands. Granul. Matter 24 (2), 48.
Xu, W.Q., Yin, Z.Y., He, S.H., Yang, N., 2024. Mechanical behavior of sand reinforced with disposable face mask chips under biaxial shear conditions. Int. J. Geomech. 24 (7), 04024115.
Xu, W.Q., Yin, Z.Y., Wang, H.L., Wang, X., 2022. Experimental study on the monotonic mechanical behavior of completely decomposed granite soil reinforced by disposable face-mask chips. J. Clean. Prod. 352, 131528.
Zhang, J.Q., Wang, X., Yin, Z.Y., Yang, N., 2022. Static and dynamic behaviors of granular soil reinforced by disposable face-mask chips. J. Clean. Prod. 331, 129838.
Zhu, C.W., Peng, C., Wu, W., 2021. Applications of micropolar SPH in geomechanics. Acta Geotech. 16, 2355–2369.
Zhu, C.W., Wu, W., Peng, C., Wang, S., Wei, X., 2024. SPH implementation of a critical state-based hypoplastic model for granular materials in large-deformation problems. Comput. Geotech. 166, 106011.